

Supplement of Atmos. Chem. Phys., 19, 9641–9661, 2019
<https://doi.org/10.5194/acp-19-9641-2019-supplement>
© Author(s) 2019. This work is distributed under
the Creative Commons Attribution 4.0 License.



Supplement of

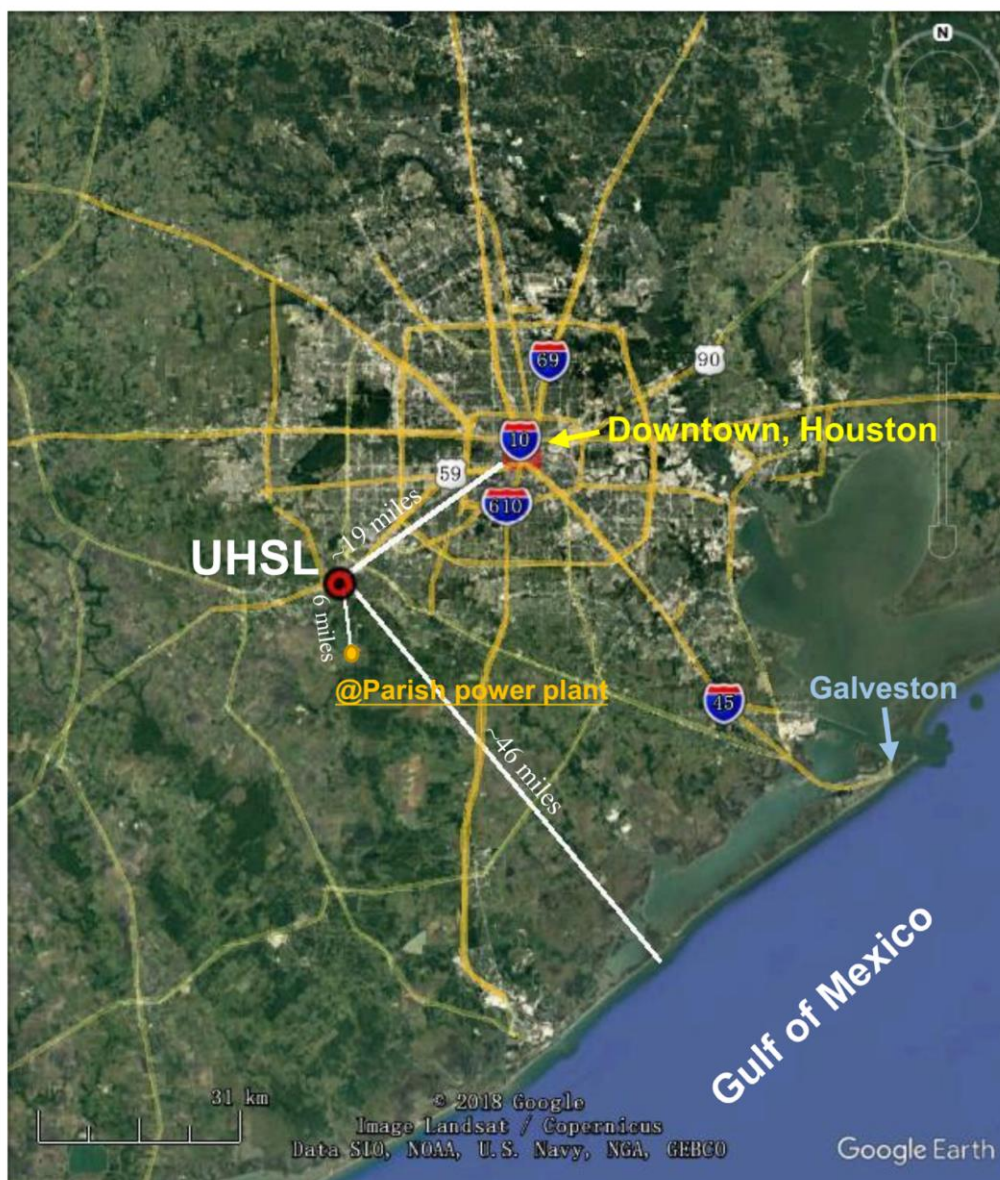
Seasonal differences in formation processes of oxidized organic aerosol near Houston, TX

Qili Dai et al.

Correspondence to: Yinchang Feng (fengyc@nankai.edu.cn)

The copyright of individual parts of the supplement might differ from the CC BY 4.0 License.

1 **1. Location of Measurement Site**



2
3 **Figure S1.** Google map for the location of the measurement site (University of Houston Sugar
4 Land, UHSL).

5

6 **2. Detection limits**

7 The detection limits for major NR-PM₁ species measured during the two campaigns were
8 calculated as three times of the standard deviation of filter periods.

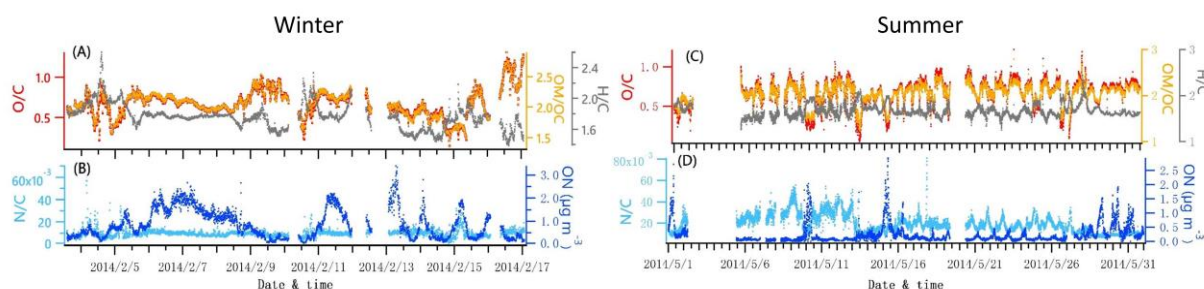
9 **Table S1.** Detection limits (DL) determined for NR-PM₁ species measured during the winter
10 and summer campaign.

		Org.	SO ₄	NO ₃	NH ₄	Chl
Winter	DL	0.106	0.008	0.008	0.001	0.008
	Measurement below DL	0%	0%	0%	0%	5%
Summer	DL	0.120	0.012	0.016	0.011	0.011
	Measurement below DL	0%	0%	3%	0%	50%

11

12

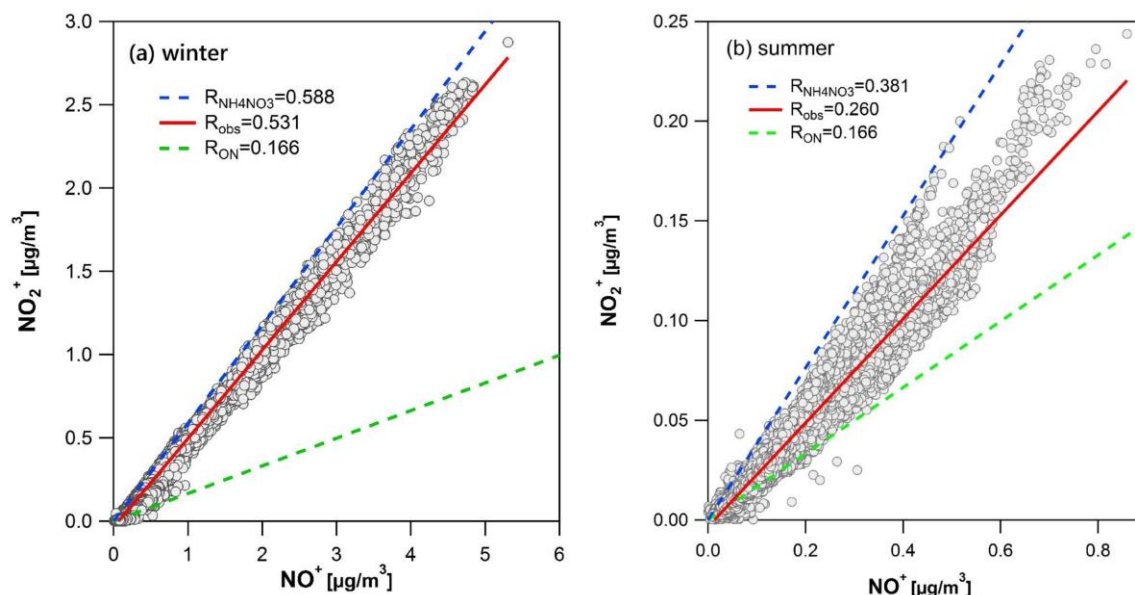
13 **3. Time series of elemental ratios and ON**



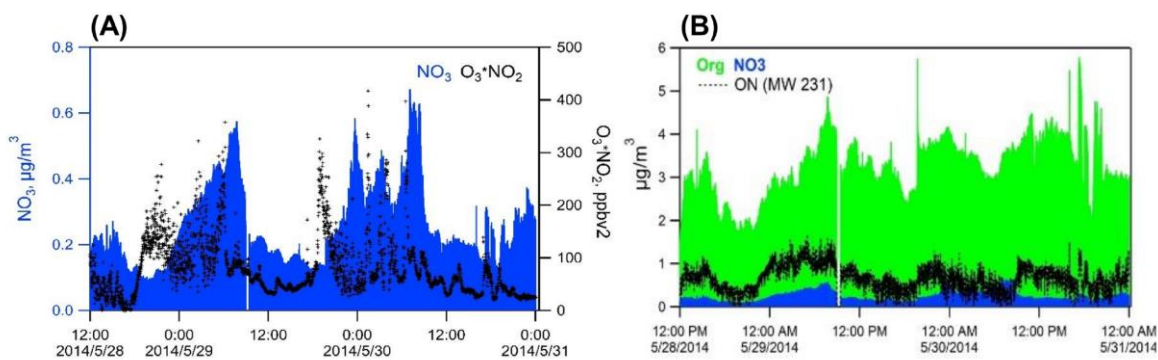
14
15 **Figure S2.** Time series of O/C, H/C, OM/OC, N/C and ON.

16
17 **4. High organic nitrate mass loading periods**

18 Figure S3 presents the scatter plots of NO_2^+ versus NO^+ for winter and summer campaigns.
19 The slope for organic nitrate (dashed green lines, $R_{\text{ON}} = 0.166$) was adopted from the literature
20 (Fry et al., 2009), the slope for inorganic nitrate (dashed blue line, $R_{\text{NH}_4\text{NO}_3} = 0.588$, 0.381 for
21 the winter and summer campaigns, respectively) was obtained from our calibrations, and R_{obs} is
22 the ambient NO_x^+ ratio. Most of the data observed in winter were far from the organic nitrate
23 slope and most of the data observed in summer close to the organic nitrate slope, indicating
24 nitrate in winter was nearly all inorganic and nitrate in summer was at least partly organic.



25
26 **Figure S3.** Scatter plots of NO_2^+ vs NO^+ for the winter and summer campaigns.



High ON loading period from May 28th to 31th

28
 29 **Figure S4.** A high ON mass loading period observed during the summer campaign: (A) time
 30 series of the mass loading of NO_3 and $\text{O}_3 \cdot \text{NO}_2$, (B) organics (Org), NO_3 and estimated ON.
 31

32 **Table S2.** Results of organic nitrates estimated using the NO_x^+ ratio method.

	$\text{NO}_{3,\text{ON}}$ conc. ($\mu\text{g m}^{-3}$)		$\text{NO}_{3,\text{ON}}/\text{NO}_{3,\text{obs}}$		ON/OA	
	lower	upper	lower	upper	lower	upper
Winter	0.22	0.34	34%	35%	31%	66%
Summer	0.05	0.06	61%	81%	9%	17%

33
 34 **5. PMF Analysis**
 35 **5.1 Selection of PMF factor number**
 36 First, a minimum error value was applied to the error matrix, and each ion was evaluated
 37 by its signal-to-noise (SNR) ratio. Mass fragments with an average SNR between 0.2 and 2
 38 were downweighted by increasing their errors by a factor of 2, while those mass fragments with
 39 a $\text{SNR} < 0.2$ were removed from the dataset. Errors of the ions related to CO_2^+ (i.e., O^+ , HO^+ ,
 40 H_2O^+ , CO^+) were also downweighted to avoid excessive weighting of the signal at m/z 44. All
 41 isotopes were removed from the matrix given that their signals were scaled to their parent ions.
 42 The PMF2 algorithm running in robust mode with the error model set to 0 was used for PMF
 43 analysis.

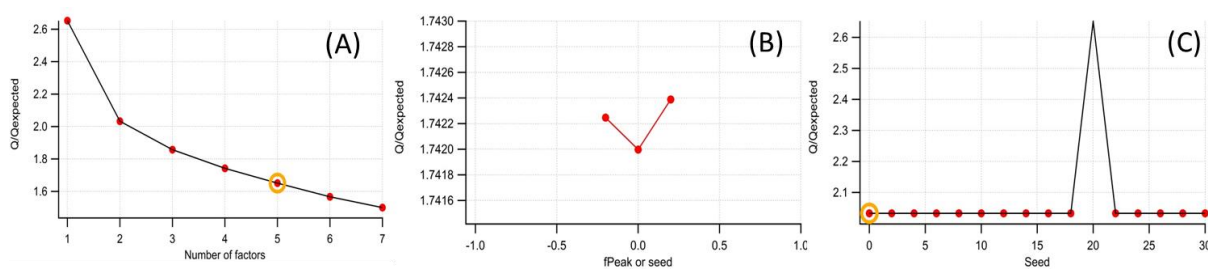
44 The PMF solution with factor numbers greater than five and four for the winter and
 45 summer, respectively, yielded no new distinct and physical meaningful factors. The Q/Q_{exp}
 46 and the factors obtained for different FPEAK (from -1 to 1 with an increment of 0.2) values

47 resulted in small differences in the OA components. Because of the lowest Q/Q_{exp} and because
48 the use of FPEAK values different from zero did not improve the correlations between PMF
49 factors and external tracers, the five- and four-factor solutions with FPEAK = 0 can be well
50 interpreted in winter and summer, respectively. The convergence of the PMF model containing
51 five and four factors were examined by running each model from fifteen different starting
52 values (SEEDs 0-30 with a step value of 2). The small variation observed in Q/Q_{exp} and the
53 mass fraction of different factors as SEED changed indicates the solutions were stable. As a
54 result, SEED 0 was chosen for the final solution.

55 OA in winter

56 The values of Q/Q_{exp} of the PMF solution with more than three factors slightly decreased
57 when adding a new factor into the model, indicating that the best solution probably contained at
58 least three factors (Fig. S5). Comparing with the three-factor solution, the reconstructed OA
59 mass with factor number great than three fitted the measured OA mass very well, and the
60 six-factor solution had the smallest scaled residuals for ions (Fig. S6). Thus, PMF solutions
61 containing between four and six factors could explain most of the variance of the winter dataset
62 (Fig. S7).

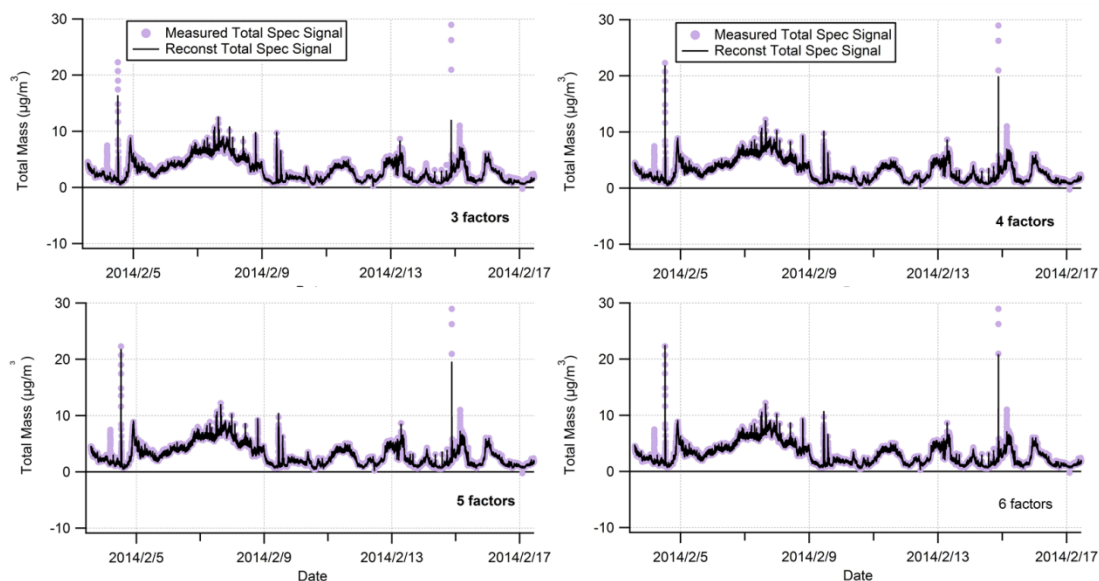
63



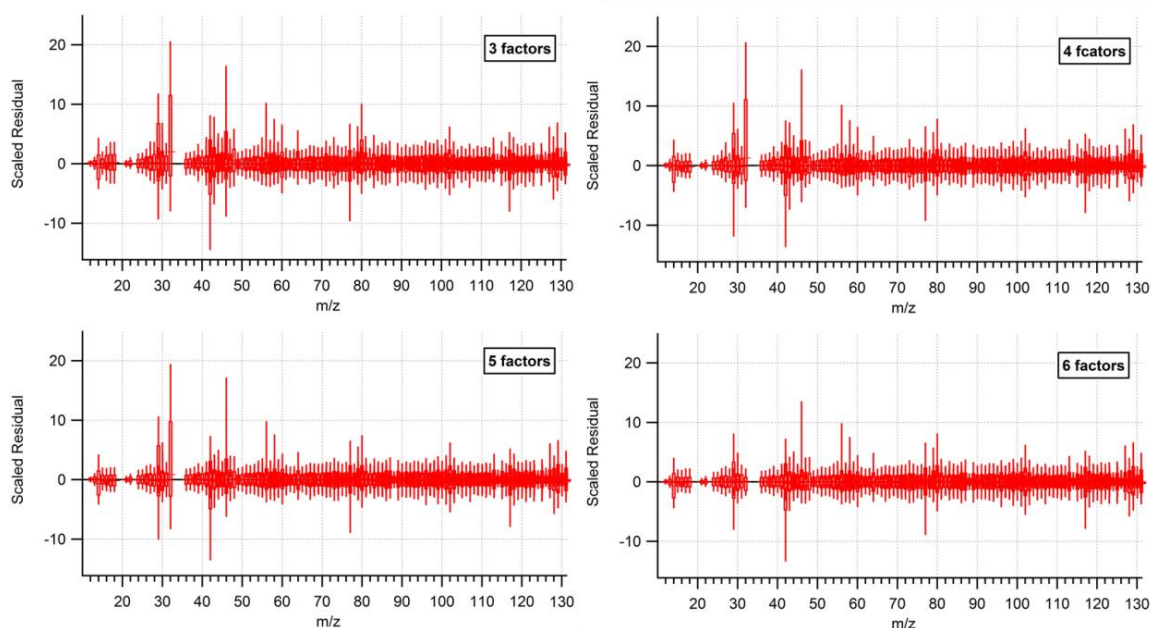
64

65 **Figure S5.** Q/Q_{exp} for PMF solutions containing between one to seven factors for the winter
66 dataset (A). Q/Q_{exp} for the five-factors solution with FPEAK from -1 to 1 (B). Q/Q_{exp} for the
67 five-factors solution with SEED from 0-30 (C).

68

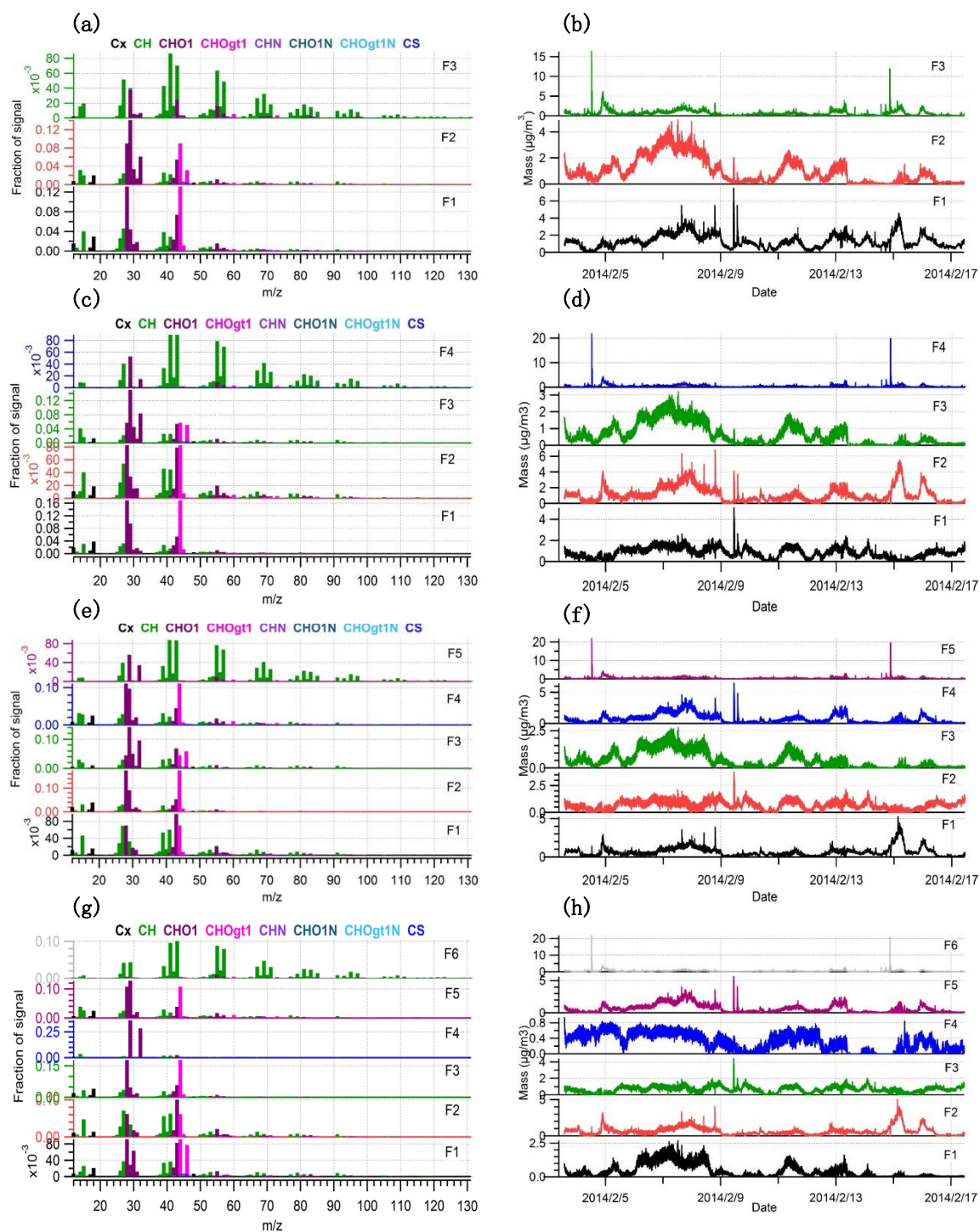


69
 70 **Figure S6.** Measured and reconstructed submicron OA mass concentrations by PMF solutions
 71 containing three to six factors for the winter dataset.



73
 74 **Figure S7.** Scaled residuals for PMF models including three to six factors for the winter
 75 dataset.

76
 77 By comparing the mass spectra of factors in the five-factor solution with that in the six-factor
 78 solution (Fig. S8), we find that F5 in the five-factor solution was split into F4 and F6 in the
 79 six-factor solution. As observed in Table S3, F4 in the six-factor solution is an unrealistic factor
 80 with both high H:C and O:C ratios, which is not physically meaningful.



81
 82 **Figure S8.** Comparison of mass spectra and time series for three- (a, b), four- (c, d), five- (e, f),
 83 and six- (g, h) factor PMF solutions of the winter dataset.

84
 85

86 **Table S3.** H:C, O:C and OM:OC ratios of factors resulting from PMF solutions including three
 87 to six factors (F1 to F6) for the winter dataset.

Number of factors in PMF solution	H:C/ O:C/ OM:OC					
	F1	F2	F3	F4	F5	F6
3	1.52/0.72/2.10	1.84/0.99/2.49	2.03/0.11/1.33			
4	1.45/1.07/2.56	1.65/0.49/1.80	1.99/0.95/2.45	2.15/0.09/1.31		
5	1.68/0.37/1.65	1.41/1.10/2.61	2.06/0.89/2.38	0.61/0.76/2.17	2.17/0.11/1.34	
6	1.64/0.71/2.11	1.69/0.35/1.61	1.37/0.95/2.40	2.92/1.52/3.28	1.63/0.85/2.28	2.06/0.04/1.23

88
 89 As defined in Equation S1, the spectral overlapping fraction (SOF) derived from the
 90 spectral contrast angle between factors can be used to access the degree of similarity between
 91 the mass spectra of PMF factors (Wan et al., 2002; Wallace et al., 2018). SOF varies between 0
 92 and 1 for factors with null and complete mass spectrum overlap, respectively.

$$93 \text{ SOF} = 1 - \frac{\text{SCA}}{90} \quad (\text{S1})$$

94 where SCA is the spectral contrast angle between PMF factors (with value of degrees).

95 The six-factor PMF solution exhibits higher resemblance between factors as reflected by
 96 SOFs values exceeding 0.9 for F1 and F2, as well as for F5 and F6 (Table S4). These results
 97 indicated that the optimum number of factors is likely no more than five. The PMF solutions
 98 with three to five factors have distinct chemical character as reflected by varying oxidation
 99 metrics and spectral overlapping fractions not exceeding 0.9. Although the SOF value for F1
 100 and F3 in the five-factor solution is as high as 0.9, the oxidation states of F1 and F3 are
 101 obviously different. Because the scaled residual for ions in the five-factor solution gets smaller
 102 than those in the four-factor solution, the five-factor solution is selected as the optimum
 103 solution for the winter dataset.

104

105 **Table S4.** Spectral overlapping fraction (SOF) between factors in PMF solutions containing
 106 three to six factors (F1 to F6) for the winter dataset.

	F1	F2	F3	F4	F5	F6	Number of factors in PMF solution
F1	1						
F2	0.58	1					4
F3	0.82	0.68	1				
F4	0.43	0.82	0.54	1			
F1	1						
F2	0.30	1					5
F3	0.90	0.33	1				
F4	0.78	0.26	0.70	1			
F5	0.45	0.46	0.47	0.35	1		
F1	1						
F2	1	1					6
F3	0.73	0.73	1				
F4	0.66	0.66	0.76	1			
F5	0.76	0.76	0.78	0.73	1		
F6	0.73	0.73	0.76	0.70	1	1	

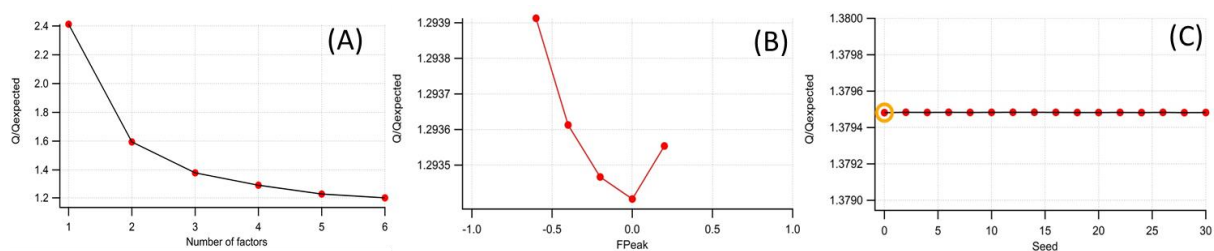
107

108 **OA in summer**

109 The value of Q/Q_{exp} consistently decreased when additional factors were added in the
 110 model. As shown in Fig. S9, after the four-factor solution, the incorporation of additional
 111 factors caused smaller decreases in Q/Q_{exp} , indicating that a four-factor solution could explain
 112 the variance of summer submicron OA. This is supported by Figs. S10 and S11, which indicate
 113 measured and reconstructed OA time series and the scaled residuals for each solution,
 114 respectively.

115

116



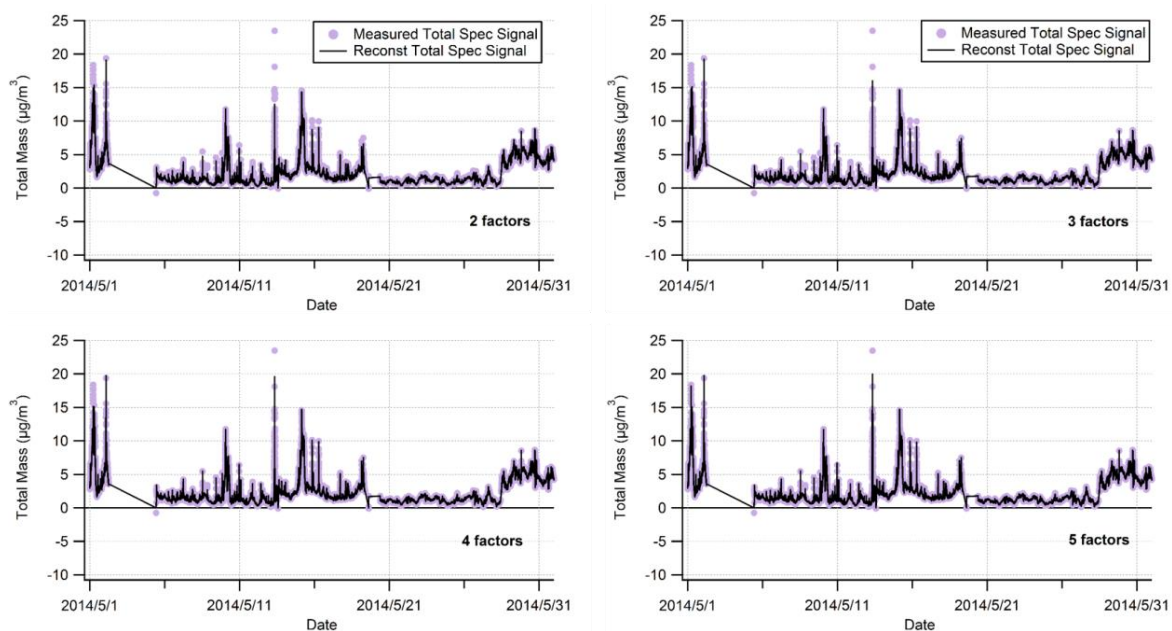
117

118 **Figure S9.** Q/Q_{exp} for PMF solutions containing one to five factors for the summer dataset (A).

119 Q/Q_{exp} for the four-factors solution with FPEAK from -1 to 1 (B). Q/Q_{exp} for the four-factors

120 solution with SEED from 0-30 (C).

121

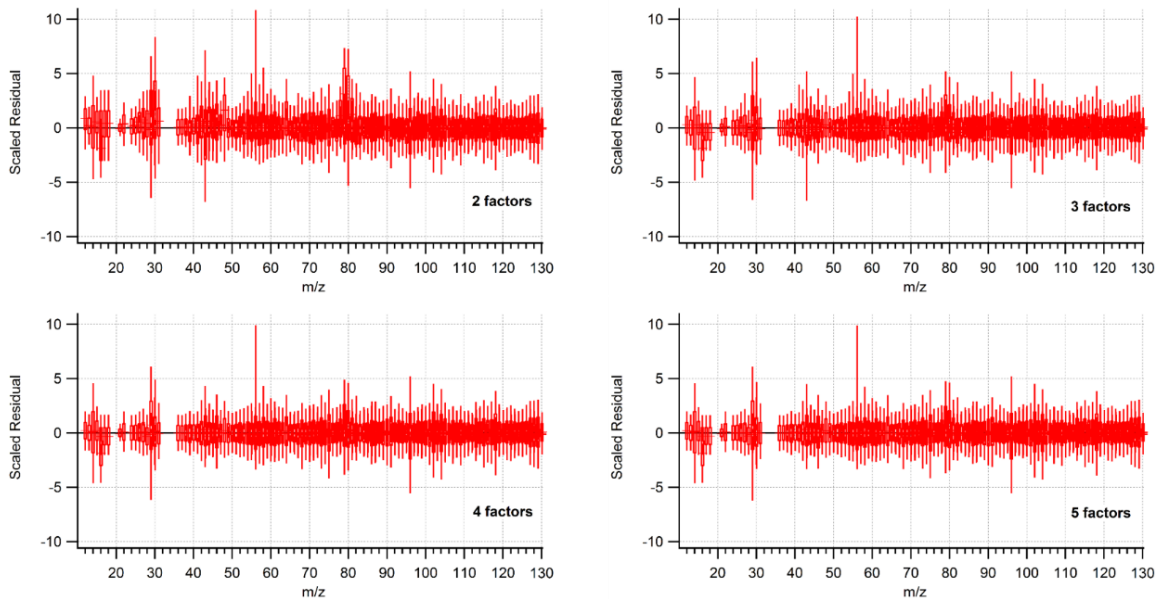


122

123 **Figure S10.** Measured and reconstructed submicron OA mass concentrations by PMF solutions

124 containing two to five factors for the summer dataset.

125



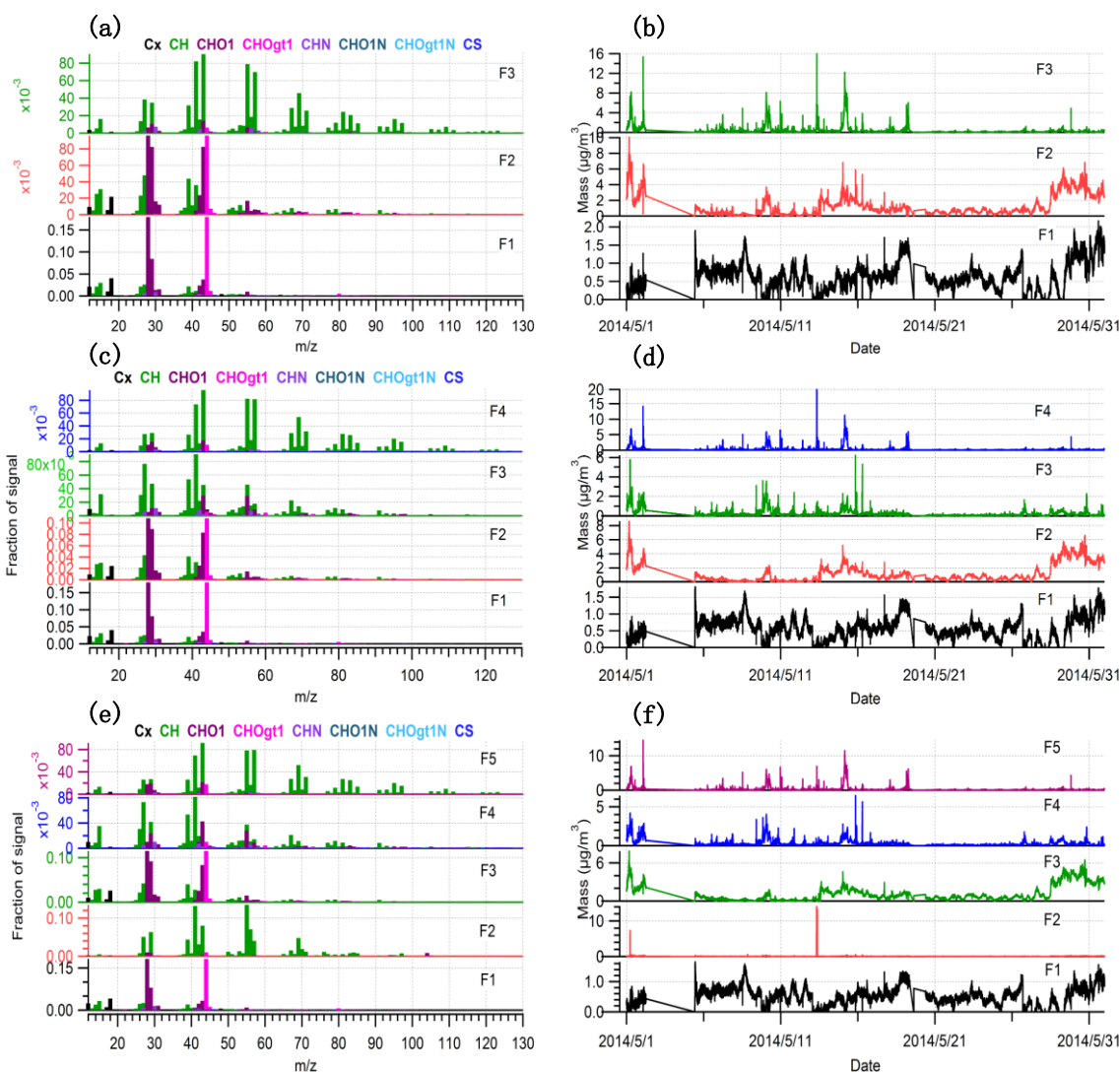
126

127 **Figure S11.** Scaled residuals for PMF models including two to five factors for the summer
 128 dataset.

129

130 The PMF factors associated with a five-factor solution were interpreted potentially as three
 131 POA (HOA, BBOA and COA) and two OOA (LO-OOA and MO-OOA) factors. Our spectral
 132 results (Fig. S12) show that F4 in the four-factor solution was split into F2 and F5 in the
 133 five-factor solution. In this case, F2 is unrealistic because the O/C ratio of F2 is lower than that
 134 of HOA (Table S5). In addition, there is no $C_3H_3O^+$ signal at m/z 55 in the mass spectra of F2,
 135 and the diel plot of F2 does not show a routine peak during local mealtime. Thus, it is unlikely
 136 to be related to cooking activities. Thus, we believe that the four-factor solution is the optimum
 137 solution for the summer dataset.

138



139
 140 **Figure S12.** Comparison of mass spectra and time series for three- (a, b), four- (c, d) and five-
 141 (e, f) factor PMF solutions of the summer dataset.

142
 143 **Table S5.** H:C, O:C and OM:OC ratios of factors resulting from PMF solutions including three
 144 to five factors (F1 to F5) for the summer dataset.

Number of factors in PMF solution	H:C/ O:C/OM:OC				
	F1	F2	F3	F4	F5
3	1.43/1.08/	1.66/0.66/	2.06/0.07/		
4	1.43/1.07/2.59	1.63/0.74/2.12	1.86/0.13/1.35	2.09/0.07/1.28	
5	1.42/1.08/2.61	2.03/0.05/1.24	1.61/0.78/2.18	1.85/0.17/1.41	2.08/0.10/1.32

145
 146 **4.2 Factor interpretation**

147 The identified factors of OA in the winter included three POA factors (a hydrocarbon-like

148 OA (HOA), a biomass burning OA (BBOA), and a cooking-related OA (COA)), and two
149 presumed SOA factors divided according to their O/C ratios (a more oxidized oxygenated OA
150 (MO-OOA) and a less oxidized oxygenated OA (LO-OOA)). However, we were unable to
151 identify a COA factor for the summer dataset.

152

153 **Hydrocarbon-like OA (HOA)**

154 As a common factor of OA, HOA has been identified in both winter and summer
155 campaigns. The mass spectra of HOA is characterized by the presence of alkyl fragments, with
156 strong signal of non-oxygenated species at m/z 43 ($C_3H_7^+$), m/z 55 ($C_4H_7^+$), m/z 56 ($C_4H_8^+$) and
157 m/z 57 ($C_4H_9^+$) (main text, Fig. 6), which is generated during fossil fuel combustion (Lanz et al.,
158 2008; Morgan et al., 2010; Ng et al., 2010; Wallace et al., 2018). Strong correlations were
159 found between the time series of HOA and the $C_nH_{2n+1}^+$ and $C_nH_{2n-1}^+$ ions, e.g., $C_3H_7^+$ ($r = 0.93$
160 and 0.97 for the winter and summer dataset, respectively), $C_4H_7^+$ ($r = 0.93$ and 0.96), $C_4H_8^+$ ($r =$
161 0.94 and 0.92) and $C_4H_9^+$ ($r = 0.90$ and 0.99). The high fractions of alkyl fragments resulted in
162 the highest H/C ratio (2.17 and 2.09 for the winter and summer) and lowest O/C ratio (0.11 and
163 0.07) of HOA compared to other factors. Additionally, both HOA factors in the summer and
164 winter correlated very well with primary combustion derived trace gas species such as CO and
165 NO (main text, Fig. 4). The HOA diurnal profiles show peaks during morning rush-hours (at
166 6-7:00 and 7-8:00 local time in summer and winter). Because Interstate Highway 69, with high
167 traffic flow, is located very close to the measurement site, it is expected that traffic-related
168 pollutants emitted from vehicle fleets would contribute to OA in both winter and summer. The
169 decrease of HOA in the afternoon likely was due to the dilution effect of a rising PBL (Kim et
170 al., 2017). The HOA increased from late afternoon (15:00-16:00) until the next morning,
171 suggesting that the shallow PBL enriched air pollutants from traffic emissions. The diurnal
172 pattern of HOA in the winter (Fig. 3, main text) was characterized with a peak during evening
173 rush hour, indicating the enhanced association of HOA with vehicle emissions.

174

175 **Biomass burning OA (BBOA)**

176 The BBOA factor was identified using factor-tracer correlation. The commonly used tracer
177 of biomass burning is levoglucosan ($C_6H_{10}O_5$), which has significant signal of fragment ions at

178 $C_2H_4O_2^+$ (m/z 60) and $C_3H_5O_2^+$ (m/z 73) (Cubison et al., 2011). These m/z ions have been
179 widely used as tracers for BBOA in AMS datasets (Cubison et al., 2011; Zhang et al., 2011;
180 Kim et al., 2017; Wallace et al., 2018). The ion signal of $C_2H_4O_2^+$ in mass spectra of BBOA is
181 higher than that in HOA and COA for our dataset (main text, Fig. 6). Fig. 4 (main text) presents
182 strong correlations between BBOA and $C_2H_4O_2^+$, with Pearson's r of 0.96 and 0.68 for the
183 winter and summer dataset, respectively.

184 The mass spectra of BBOA was characterized by strong correlation with alkyl fragments
185 ($C_nH_{2n+1}^+$ and $C_nH_{2n-1}^+$: $C_4H_8^+$ $r = 0.66$ and 0.77 for winter and summer, respectively) and with
186 oxygenated ions ($C_xH_yO^+$ and $C_xH_yO_2^+$: $C_6H_{10}O^+$ $r=0.75$ and 0.96 for winter and summer
187 dataset, respectively). Sources of BBOA include wood combustion for cooking and heating,
188 waste disposal, and wildfires. BBOA corresponds to local emissions under relatively low wind
189 speed or regional transport under relatively high wind speed. This finding is consistent with a
190 previous study conducted in another site in Houston (Wallace et al., 2018). BBOA can
191 gradually age during transport, leading to a broad range of O/C. The O/C ratio of BBOA is
192 higher than that in HOA and lower than that in both OOA factors in both seasons, but the O/C
193 of BBOA in winter (0.76) is several times of that in summer (0.13), likely indicating that
194 BBOA in winter is from different sources and/or processed to some extent. The diurnal pattern
195 of BBOA (Fig. 3, main text) shows overnight increases in winter, with peaks at mealtime in the
196 morning and evening in summer. A possible reason for this difference is that wood burning
197 during winter was used not only for cooking but also for heating, especially in the more rural
198 northern areas of Houston, from which PM was transported. BBOA was the most abundant OA
199 in Houston during the winter campaign, revealing the important role of residential activities in
200 OA enhancement.

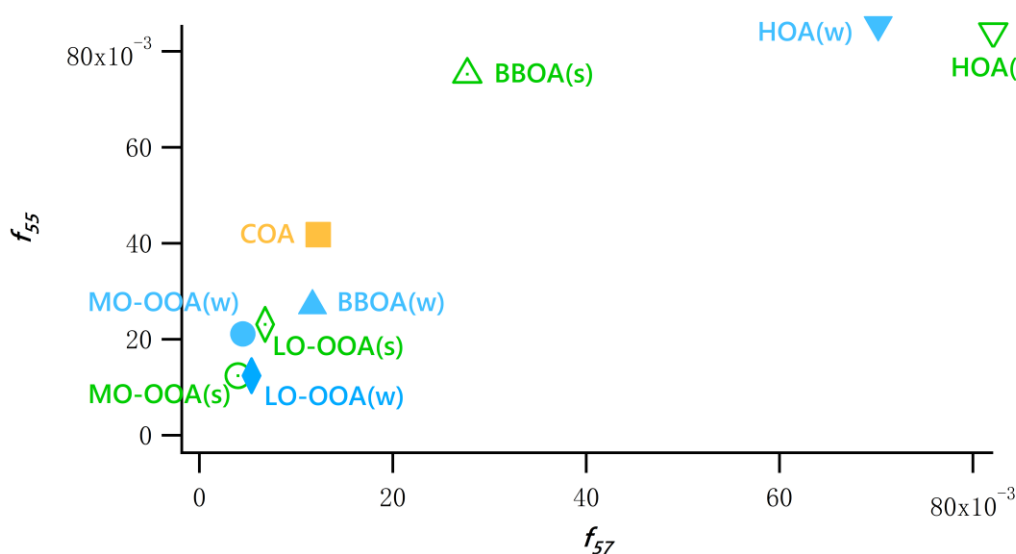
201

202 **Cooking OA (COA)**

203 COA was responsible for 22% of OA mass in winter, which is higher than HOA. However,
204 COA was not identified during the summer campaign. The mass spectrum of COA is similar to
205 that of HOA but exhibits more oxidized features. The O/C ratio for COA is 0.37, which is
206 larger than that for HOA by a factor of three. Previous studies suggest that $C_3H_3O^+$ could be
207 used as key tracer of cooking-related aerosols, as it is likely the fragment of oxygenated fatty

208 acids in cooking oils and animal fat (He et al., 2010; Mohr et al., 2012). The abundance of
 209 $C_3H_3O^+$ ions in m/z 55 in COA was higher than that in other factors (main text, Fig. 7).
 210 Moderate correlation ($r= 0.65$) between the time series of COA and $C_3H_3O^+$ was found.
 211 Additionally, the signals for m/z 55 to m/z 57 for COA in the summer are close to those for
 212 LO-OOA and MO-OOA and higher than those for BBOA and HOA (Fig. S13), which provides
 213 insight into the difference in mass spectra between COA and other POA (Zhang et al., 2011;
 214 Mohr et al., 2012). No routine peak was found during mealtimes in the diurnal pattern of COA
 215 (Fig. 3, main text). There is a coal-fired restaurant situated northeast of the measurement site
 216 (UHSL). The northeasterly winds were observed at the measurement site with a high frequency
 217 during the winter campaign but the summer (Fig. 1), which is likely to responsible for the
 218 impact of emissions from cooking activities on this site during winter, making the COA factor
 219 unable to be identified in the summer.

220



221
 222 **Figure S13.** f_{55} vs. f_{57} of PMF factors for the winter and summer periods. (w) and (s) denote
 223 the winter and summer data, respectively.

224

225 Less-Oxygenated OOA (LO-OOA)

226 As a ubiquitous factor of OA, LO-OOA was identified for the two campaigns in our study.
 227 The mass spectra of LO-OOA contains less oxidized fragments as compared to MO-OOA
 228 (main text, Fig. 6). LO-OOA correlated well with CHO_{gt1} fragments in both seasons. As a

229 proxy for fresh SOA, LO-OOA featured a low f_{44} compared to MO-OOA. The O/C ratios for
 230 LO-OOA in the winter and summer are 0.89 and 0.74, respectively, which are lower than that
 231 for MO-OOA, but higher than that for BBOA and COA. The strong correlation between
 232 LO-OOA and NO_3^- ($r = 0.75$ and 0.64 for winter and summer data) further confirmed its
 233 secondary nature. In addition, LO-OOA was correlated very well with ON in the summer, with
 234 Pearson's correlation coefficient of 0.73 (main text, Fig. 4). These results together confirmed
 235 the fresher nature of LO-OOA. LO-OOA accounted for 18% and 53% of OA mass in the winter
 236 and summer, respectively.

237

238 **More-Oxygenated OOA (MO-OOA)**

239 MO-OOA has a higher O:C ratio than LO-OOA. The mass spectrum of MO-OOA is
 240 comprised of the CHO^+ and $\text{CHO}_{\text{gt}1}$ families. Fig. 4 (main text) shows strong covariance
 241 between MO-OOA and CO_2^+ . In addition, MO-OOA is moderately correlated with O_3 and SO_4^{2-} ,
 242 which confirms the identity of this factor. Both LO-OOA and MO-OOA have been observed in
 243 the winter and summer, indicating OOA is a ubiquitous component of OA, as reported in the
 244 literature (Ng et al., 2010). MO-OOA appears to have a notable association with regional
 245 transport as its high concentrations occurred with relatively high wind speed.

246

247 **6. Effects of Photochemistry and Aqueous-phase Processing on SOA Formation**

248 Tables S6-S9 present results of the Dunn-Bonferroni *post hoc* test for bin pairwise
 249 comparisons. The data associated with the artificially created bins in both seasons did not pass
 250 the normal test and homogeneity test of variances. The Kruskal-Wallis ANOVA for winter and
 251 summer data of the bins were significant. Thus, the Dunn-Bonferroni test was performed for
 252 the *post-hoc* pairwise comparisons. The difference between measured variables in different bins
 253 were significant if the $p' \leq 0.05$.

254

255 **Table S6.** Result of the Dunn-Bonferroni *post hoc* test for the pairwise comparisons of
 256 variables in different LWC bins measured in the winter campaign. Values (p') denote adjusted
 257 significance: $p' = p/n = p/15$.

LWC	0-5	5-10	10-15	15-20	20-30
-----	-----	------	-------	-------	-------

		(µg m ⁻³)				
RH	20-40	<2E-16				
	40-60	<2E-16	5.80E-02			
	60-80	<2E-16	4.53E-11	1.07E-06		
	80-100	<2E-16	7.33E-08	1.33E-05	6.56E-02	
	100-120	<2E-16	6.00E-15	3.93E-11	9.89E-03	5.03E-02
WS	20-40	3.67E-15				
	40-60	4.20E-15	2.23E-02			
	60-80	8.67E-14	6.67E-02	-4.62E-02		
	80-100	7.33E-11	3.68E-02	6.66E-02	-4.93E-02	
	100-120	3.60E-15	3.60E-06	3.17E-03	7.33E-05	2.47E-02
LO-OOA	20-40	<2E-16				
	40-60	3.33E-15	9.10E-03			
	60-80	6.07E-05	2.00E-10	2.95E-04		
	80-100	6.37E-02	8.00E-10	2.13E-05	4.37E-02	
	100-120	5.73E-02	2.60E-15	4.33E-11	4.94E-04	4.73E-02
MO-OOA	20-40	3.09E-04				
	40-60	4.13E-04	6.52E-02			
	60-80	8.00E-06	3.09E-02	6.14E-02		
	80-100	9.33E-06	5.13E-03	2.02E-02	5.26E-02	
	100-120	2.27E-12	1.73E-06	9.60E-05	2.53E-03	5.52E-02

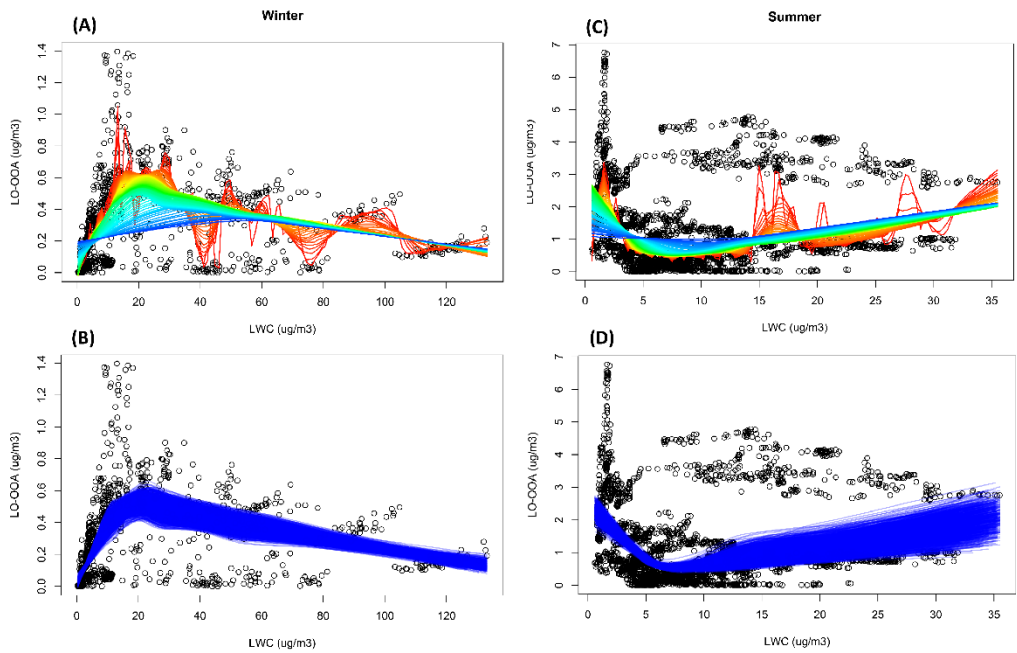
258

259

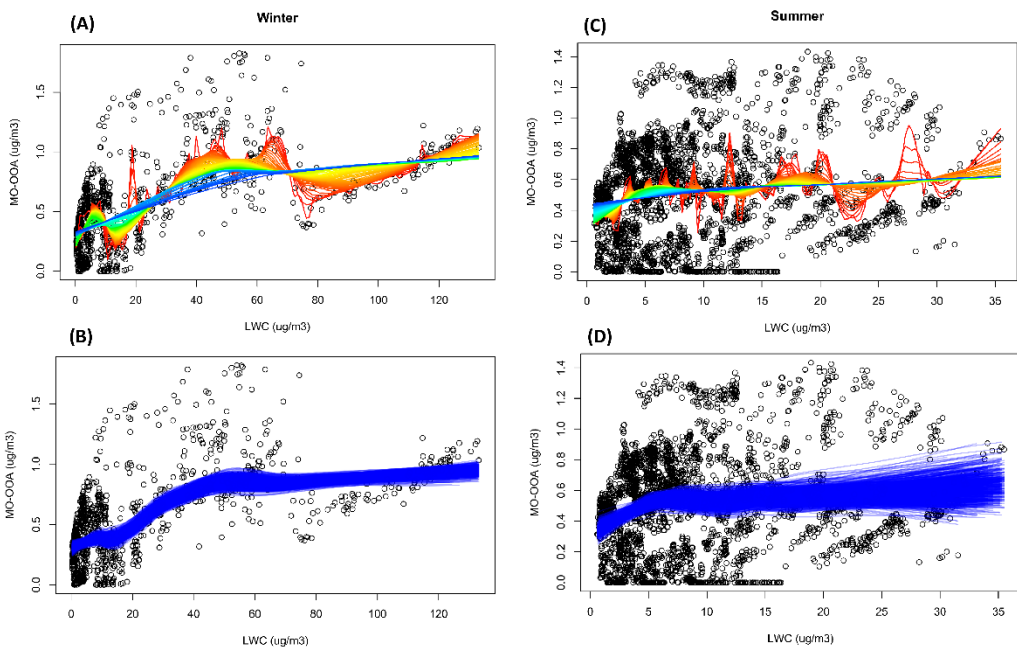
260 **Table S7.** Result of the Dunn-Bonferroni *post hoc* test for the pairwise comparisons of
 261 variables in different LWC bins measured in the summer campaign. Values (p') denote adjusted
 262 significance: $p' = p/n = p/15$.

	LWC ($\mu\text{g m}^{-3}$)	0-10	10-20	20-30	30-40	40-50
RH	10-20	<2E-16				
	20-30	<2E-16	1.79E-02			
	30-40	<2E-16	6.44E-02	6.43E-02		
	40-50	<2E-16	6.87E-03	6.33E-02	4.45E-02	
	50-60	<2E-16	9.33E-11	9.20E-05	2.20E-05	1.09E-02
WS	10-20	<2E-16				
	20-30	<2E-16	-3.87E-04			
	30-40	<2E-16	1.97E-03	6.67E-02		
	40-50	<2E-16	4.46E-03	6.67E-02	6.67E-02	
	50-60	<2E-16	1.13E-04	6.59E-02	6.65E-02	6.66E-02
LO-OOA	10-20	<2E-16				
	20-30	<2E-16	1.67E-07			
	30-40	<2E-16	6.67E-14	4.54E-03		
	40-50	<2E-16	3.67E-15	3.27E-05	4.48E-02	
	50-60	<2E-16	3.60E-15	4.47E-07	2.51E-02	6.67E-02
MO-OOA	10-20	5.61E-02				
	20-30	2.53E-05	1.27E-05			
	30-40	6.67E-02	6.65E-02	4.60E-03		
	40-50	1.80E-12	1.27E-12	5.17E-04	5.67E-08	
	50-60	<2E-16	<2E-16	3.47E-11	3.93E-15	1.48E-02

263
 264
 265



266
 267 **Figure S14.** LOWESS curves for the nighttime LO-OOA vs. LWC during winter (A) and
 268 summer (B), and for the associated resampled data obtained by bootstrap method (B for winter
 269 and D for summer).
 270



271
 272 **Figure S15.** LOWESS curves for the nighttime MO-OOA vs. LWC during winter (A) and
 273 summer (B), and for the associated resampled data obtained by bootstrap method (B for winter
 274 and D for summer).
 275

276 **Table S8.** Result of the Dunn-Bonferroni *post hoc* test for the pairwise comparisons of
 277 variables in different O_x bins measured in the winter campaign. Values (*p*) denote adjusted
 278 significance: $p' = p/n = p/15$.

	O _x (ppb)	0-10	10-20	20-30	30-40	40-50
RH	10-20	1.93E-11				
	20-30	1.27E-12	6.66E-02			
	30-40	3.73E-04	5.07E-15	<2E-16		
	40-50	3.44E-02	<2E-16	<2E-16	<2E-16	
	50-60	6.46E-02	3.73E-15	<2E-16	1.20E-12	5.34E-02
Radiometer	10-20	1.60E-10				
	20-30	1.20E-03	5.53E-15			
	30-40	3.27E-10	4.97E-02	<2E-16		
	40-50	3.07E-15	8.00E-09	<2E-16	<2E-16	
	50-60	4.33E-15	1.13E-10	<2E-16	3.33E-15	2.80E-03
LO-OOA	10-20	6.67E-02				
	20-30	4.80E-07	<2E-16			
	30-40	3.53E-08	<2E-16	1.40E-02		
	40-50	5.73E-02	4.13E-02	<2E-16	<2E-16	
	50-60	2.47E-02	8.00E-03	<2E-16	<2E-16	3.73E-02
MO-OOA	10-20	6.64E-02				
	20-30	4.20E-11	<2E-16			
	30-40	4.07E-15	<2E-16	<2E-16		
	40-50	7.33E-08	3.93E-15	1.87E-04	<2E-16	
	50-60	6.53E-14	3.80E-15	6.67E-04	4.68E-03	1.07E-06

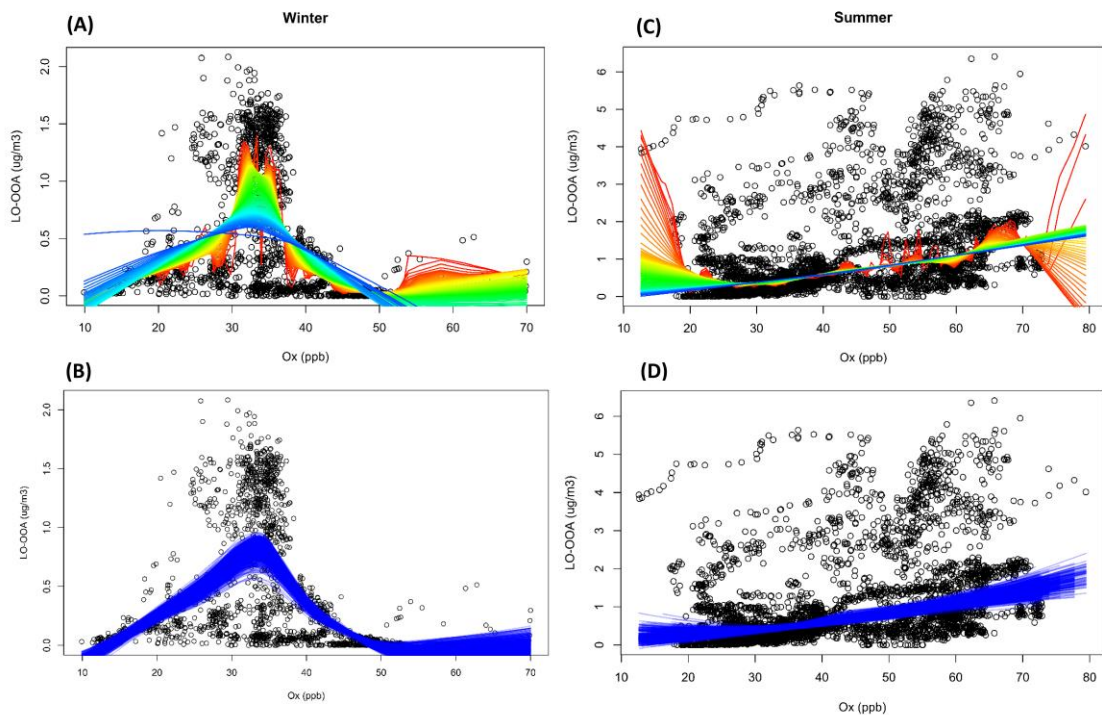
279

280

281 **Table S9.** Result of the Dunn-Bonferroni *post hoc* test for the pairwise comparisons of
 282 variables in different O_x bins measured in the summer campaign. Values (*p*') denote adjusted
 283 significance: $p' = p/n = p/15$.

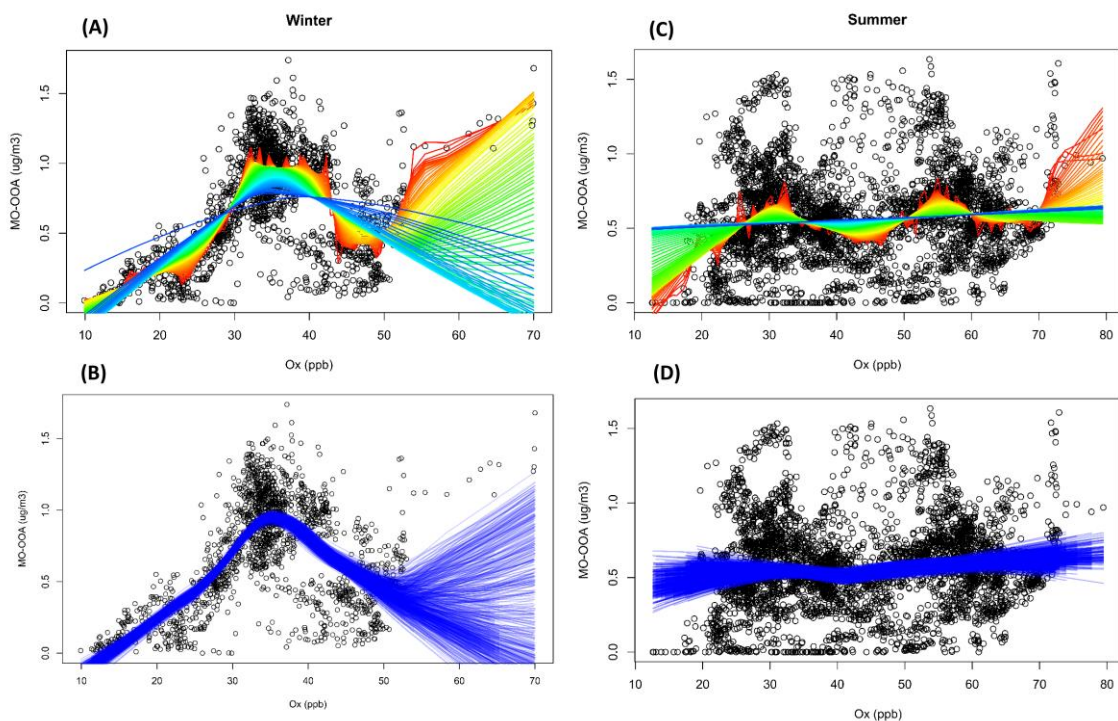
	O _x (ppb)	0-20	20-30	30-40	40-50	50-60
RH	20-30	5.20E-15				
	30-40	<2E-16	<2E-16			
	40-50	<2E-16	<2E-16	1.20E-03		
	50-60	<2E-16	<2E-16	<2E-16	5.07E-15	
	60-70	<2E-16	<2E-16	<2E-16	<2E-16	<2E-16
Radiometer	20-30	3.40E-15				
	30-40	<2E-16	<2E-16			
	40-50	<2E-16	1.67E-15	2.20E-06		
	50-60	<2E-16	<2E-16	1.47E-03	2.53E-13	
	60-70	<2E-16	<2E-16	<2E-16	<2E-16	<2E-16
LO-OOA	20-30	2.20E-04				
	30-40	6.66E-03	3.67E-15			
	40-50	<2E-16	<2E-16	<2E-16		
	50-60	<2E-16	<2E-16	<2E-16	6.62E-02	
	60-70	<2E-16	<2E-16	<2E-16	5.33E-07	1.20E-08
MO-OOA	20-30	1.33E-11				
	30-40	2.87E-15	8.33E-05			
	40-50	4.07E-15	7.57E-04	6.67E-02		
	50-60	<2E-16	<2E-16	<2E-16	4.13E-15	
	60-70	2.73E-15	7.33E-06	4.03E-02	4.20E-02	8.00E-13

284
 285
 286
 287



288

289 **Figure S16.** LOWESS curves for the daytime LO-OOA vs. O_x during winter (A) and
 290 (B), and for the associated resampled data obtained by bootstrap method (B for winter and D
 291 for summer).



292

293 **Figure S17.** LOWESS curves for the daytime MO-OOA vs. LWC during winter (A) and
 294 summer (B), and for the associated resampled data obtained by bootstrap method (B for winter
 295 and D for summer).

296 **References**

- 297 Cubison, M. J., Ortega, A. M., Hayes, P. L., Farmer, D. K., Day, D., Lechner, M. J., Brune, W.
298 H., Apel, E., Diskin, G. S., Fisher, J. A., Fuelberg, H. E., Hecobian, A., Knapp, D. J.,
299 Mikoviny, T., Riemer, D., Sachse, G. W., Sessions, W., Weber, R. J., Weinheimer, A. J.,
300 Wisthaler, A., and Jimenez, J. L.: Effects of aging on organic aerosol from open biomass
301 burning smoke in aircraft and laboratory studies, *Atmos. Chem. Phys.*, 11, 12049-12064,
302 <https://doi.org/10.5194/acp-11-12049-2011>, 2011.
- 303 Fry, J. L., Kiendler-Scharr, A., Rollins, A. W., Wooldridge, P. J., Brown, S. S., Fuchs, H., Dube,
304 W., Mensah, A., dal Maso, M., Tillmann, R., Dorn, H. P., Brauers, T., and Cohen, R. C.:
305 Organic nitrate and secondary organic aerosol yield from NO₃ oxidation of beta-pinene
306 evaluated using a gas-phase kinetics/aerosol partitioning model, *Atmos. Chem. Phys.*, 9,
307 1431-1449, <https://doi.org/10.5194/acp-9-1431-2009>, 2009.
- 308 He, L. Y., Lin, Y., Huang, X. F., Guo, S., Xue, L., Su, Q., Hu, M., Luan, S. J., and Zhang, Y. H.:
309 Characterization of high-resolution aerosol mass spectra of primary organic aerosol
310 emissions from Chinese cooking and biomass burning, *Atmos. Chem. Phys.*, 10,
311 11535-11543, <https://doi.org/10.5194/acp-10-11535-2010>, 2010.
- 312 Kim, H., Zhang, Q., Bae, G. N., Kim, J. Y., and Lee, S. B.: Sources and atmospheric processing
313 of winter aerosols in Seoul, Korea: insights from real-time measurements using a
314 high-resolution aerosol mass spectrometer, *Atmos. Chem. Phys.*, 17, 2009-2033,
315 <https://doi.org/10.5194/acp-17-2009-2017>, 2017.
- 316 Lanz, V. A., Alfarra, M. R., Baltensperger, U., Buchmann, B., Hueglin, C., Szidat, S., Wehrli, M.
317 N., Wacker, L., Weimer, S., Caseiro, A., Puxbaum, H., Prevot, A. S. H.: Source Attribution
318 of Submicron Organic Aerosols during Wintertime Inversions by Advanced Factor
319 Analysis of Aerosol Mass Spectra. *Environ. Sci. Tech.*, 42, (1), 214-220,
320 <https://doi.org/10.1021/es0707207>, 2008.
- 321 Mohr, C., DeCarlo, P. F., Heringa, M. F., Chirico, R., Slowik, J. G., Richter, R., Reche, C.,
322 Alastuey, A., Querol, X., Seco, R., Peñuelas, J., Jiménez, J. L., Crippa, M., Zimmermann,
323 R., Baltensperger, U., and Prévôt, A. S. H.: Identification and quantification of organic
324 aerosol from cooking and other sources in Barcelona using aerosol mass spectrometer data,
325 *Atmos. Chem. Phys.*, 12, 1649-1665, <https://doi.org/10.5194/acp-12-1649-2012>, 2012.
- 326 Morgan, W. T., Allan, J. D., Bower, K. N., Highwood, E. J., Liu, D., McMeeking, G. R.,
327 Northway, M. J., Williams, P. I., Krejci, R., and Coe, H.: Airborne measurements of the
328 spatial distribution of aerosol chemical composition across Europe and evolution of the

329 organic fraction, *Atmos. Chem. Phys.*, 10, 4065-4083,
330 <https://doi.org/10.5194/acp-10-4065-2010>, 2010.

331 Ng, N. L., Canagaratna, M. R., Zhang, Q., Jimenez, J. L., Tian, J., Ulbrich, I. M., Kroll, J. H.,
332 Docherty, K. S., Chhabra, P. S., Bahreini, R., Murphy, S. M., Seinfeld, J. H., Hildebrandt,
333 L., Donahue, N. M., DeCarlo, P. F., Lanz, V. A., Prevot, A. S. H., Dinar, E., Rudich, Y., and
334 Worsnop, D. R.: Organic aerosol components observed in Northern Hemispheric datasets
335 from Aerosol Mass Spectrometry, *Atmos. Chem. Phys.*, 10, 4625-4641,
336 <https://doi.org/10.5194/acp-10-4625-2010>, 2010.

337 Wallace, H. W., Sanchez, N. P., Flynn, J. H., Erickson, M. H., Lefer, B. L., and Griffin, R. J.:
338 Source apportionment of particulate matter and trace gases near a major refinery near the
339 Houston Ship Channel, *Atmos. Environ.*, 173, 16-29,
340 <https://doi.org/10.1016/j.atmosenv.2017.10.049>, 2018.

341 Wan, K. X., Vidavsky, I., and Gross, M. L.: Comparing similar spectra: From similarity index
342 to spectral contrast angle, *J. Am. Soc. Mass Spectr.*, 13, 85-88,
343 [http://doi.org/10.1016/S1044-0305\(01\)00327-0](http://doi.org/10.1016/S1044-0305(01)00327-0), 2002.

344 Zhang, Q., Jimenez, J. L., Canagaratna, M. R., Ulbrich, I. M., Ng, N. L., Worsnop, D. R., and
345 Sun, Y. L.: Understanding atmospheric organic aerosols via factor analysis of aerosol mass
346 spectrometry: a review, *Anal. Bioanal. Chem.*, 401, 3045-3067,
347 <https://doi.org/10.1007/s00216-011-5355-y>, 2011.

348